https://doi.org/10.1038/s44306-024-00022-7

Slow and non-equilibrium dynamics due to electronic ferroelectricity in a strongly-correlated molecular conductor

Tatjana Thomas[1], Yassine Agarmani[1], Steffi Hartmann[1], Mark Kartsovnik[2], Natalia Kushch[3], Stephen M. Winter[4], Sebastian Schmid[5], Peter Lunkenheimer[5], Michael Lang[1] & Jens Müller[1] ✉

Ferroelectricity, where electronic degrees of freedom determine the polar order—thereby enabling fast switching and phase control—is an important research field in current condensed-matter physics. Using a combination of resistance noise and dielectric spectroscopy we investigate the nature of relaxor-type electronic ferroelectricity in the organic conductor κ-$(BETS)_2Mn[N(CN)_2]_3$, a system that represents a wider class of materials of correlated electron systems for which functionalities for organic spintronics recently have been discussed. The two complementary spectroscopies reveal a distinct low-frequency dynamics on different length scales, namely (i) an intrinsic relaxation that is typical for relaxor ferroelectrics which classifies the system as a possible new multiferroic, and (ii) two-level processes which we identify as fluctuating polar nanoregions (PNR), i.e., clusters of quantum electric dipoles that fluctuate collectively. The PNR preform above the metal insulator (MI) transition. Upon cooling through T_{MI}, a drastic increase of the low-frequency 1/*f*-type fluctuations and slowing down of the charge carrier dynamics is accompanied by the onset of strong non-equilibrium dynamics indicating a glassy transition of interacting dipolar clusters. The freezing of PNR and non-equilibrium dynamics is suggested to be a common feature of organic relaxor-type electronic ferroelectrics.

Molecular (organic) materials consisting of light atoms have attracted considerable interest in spintronics applications due to their small spin-orbit interaction leading to long spin relaxation times[1,2]. A number of different devices, mostly based on organic semiconductors[3], have been demonstrated over the past decades[4–6]. More recently, functionalities for organic spintronics have been discussed also in crystalline molecular materials, the so-called organic charge-transfer salts $(BEDT\text{-}TTF)_2X$, where the donor molecule BEDT-TTF (in short ET) represents bis(ethylenedithio)tetrathiafulvalene and *X* an acceptor molecule. Among these are nonlocal spin valve functionality in α-$(ET)_2I_3$[7], the theoretical prediction of spin-current generation in the prototypical organic Mott insulator κ-$(ET)_2Cu[N(CN)_2]Cl$[8], spin-current injection and detection in the related compound with $X = Cu[N(CN)_2]Br$[9], or giant spin polarization due to the CISS effect (chirality induced spin selectivity) in the organic superconductor $X = Cu(NCS)_2$[10]. For spintronics applications, multiferroic magnetoelectric materials[11–13], however very rare[14], are highly desirable since spin currents could be switched electrically. In this context, it is interesting to note that recently a number of organic charge-transfer salts are recognized as electronic ferroelectrics, e.g., $X = Cu[N(CN)_2]Cl$, which, as an antiferromagnet, is even multiferroic[15]. Although for this material a magnetoelectric coupling has not yet been established, the search for new candidates displaying rich physics of electric and magnetic polarization in organic materials, and the better understanding of their peculiar ferroelectric properties is highly desirable.

In electronic ferroelectricity, which has become of considerable research interest in recent years[16–23], the primary order parameter is determined by electronic degrees of freedom thereby allowing for fast switching and phase control, in contrast to conventional types of ferroelectricity where the electric polarization is caused by the displacement of ions or the ordering of permanent electric dipoles. In this context, an important mechanism for the formation of electric dipole moments is charge disproportionation in a modulated or bond-alternated dimerized lattice[16,24,25], which is why the organic dimer-Mott insulators $(ET)_2X$ are promising candidates for this

[1]Institute of Physics, Goethe University Frankfurt, Frankfurt (M), Germany. [2]Walther-Meissner-Institut, Bayerische Akademie der Wissenschaften, Garching, Germany. [3]Institute of Problems of Chemical Physics, Russian Academy of Sciences, Chernogolovka, Russia. [4]Department of Physics and Center for Functional Materials, Wake Forest University, Winston-Salem, NC, USA. [5]Experimental Physics V, Centre for Electronic Correlations and Magnetism, University of Augsburg, Augsburg, Germany. ✉e-mail: j.mueller@physik.uni-frankfurt.de

type of ferroelectricity[26,27]. In this class of quasi-two-dimensional molecular conductors, see Fig. 1, the transfer of one electron from two ET donor molecules to monovalent *X* leaves behind a partially-filled molecular orbital. A quasi-two-dimensional conduction band forms through the overlap of adajcent molecular orbitals, i.e., the charge carriers responsible for electrical conductivity have π-hole character with strong electronic correlations due to narrow bandwidth, reduced dimensionality and diminished screening of the charges. In these layered materials, the so-called κ-phase packing motif with a dimerized structure of the ET molecules, provides a favorable structure for order-disorder type electronic ferroelectricity that is driven by the charge order within the $(ET)_2$ dimers forming a triangular lattice[15,28,29]. The possible charge localization on one molecule within the dimer, caused by the interplay of on-site and inter-site Coulomb interactions, leads to quantum electric dipole moments, see a schematic in Fig. 1b. These ingredients for electronic ferroelectricity can be found in various compounds of organic charge transfer salts. However, the phenomenology regarding electric conductivity and polarization or the occurrence of magnetic ordering of the localized spin 1/2 moments can be rather different. For example, order-disporder-type electronic ferroelectricity can emerge within a Mott insulating phase enabling antiferromagnetic (AFM) order, thereby creating a multiferroic ground state[15], or coincide with a metal-insulator transition[28–30]. Furthermore, both long-range order or relaxor-type ferroelectricity, where the characteristic peak in ϵ' becomes suppressed and shifted to higher temperatures with increasing frequency, can arise[15,31–35].

It is an important general question whether relaxor-type ferroelectricity originates from a ferroelectric state, that is broken up into nano-domains due to quenched electric fields, or from a dipolar glass, i.e., freezing polar nanoregions (PNR) which form inside a dielectric matrix[36,37]. Furthermore, in theoretical studies of molecular organic conductors $(ET)_2X$ [24,25,38] it has been pointed out that for charge-driven-type ferroelectricity large temporal and spacial dielectric fluctuations are expected that may play a crucial role for the ferroelectric phase transition and the dielectric and optical properties. Important consequences that have been predicted are collective polar charge excitations and fluctuations of the latter that may cause superconductivity, and—most relevant for this work—the formation of PNR and electronic phase separation, where small polar clusters are a possible cause of the frequently observed relaxor-like ferroelectric dispersion[25]. In the case of the present organic charge-transfer salts $(ET)_2X$, the PNR are considered to consist of short-range domains of electric dipoles localized on the $(ET)_2X$ dimers that fluctuate collectively[38,39]. Important in this context are also the theoretical suggestions that slow dynamics and charge glassiness is intrinsic to the extended Hubbard model describing the charges on a frustrated triangular lattice[40] and that the anomalies in $\epsilon'(\omega, T)$ are due to the vicinity of a ferroelectric quantum critical point[41]. Finally, besides in equilibrium measurements, recent terahertz-field-induced polar charge order has been reported, where electronic ferroelectricity is induced by the collective inter-molecular charge transfers in each dimer[23].

In this work, we aim to address these questions of the nature of collective excitations in charge-driven ferroelectric phases and their coupling to electric fields by exemplarily studying the relatively new system κ-$(BETS)_2Mn[N(CN)_2]_3$, where BETS is a variant of ET in which the four inner sulfur atoms are replaced by selenium, exhibiting a metal-insulator transition at $T_{MI} \approx 20$–25 K[42,43]. Besides characterizing the transition by thermal expansion and electrical resistivity measurements we apply a unique combination of resistance noise spectroscopy and dielectric spectroscopy revealing microscopic evidence for fluctuating PNR as collective excitations and precursors of relaxor ferroelectricity. Their slow dynamics strongly depends on temperature and couples to the electric field. We identify the insulating state below T_{MI} as ferroelectric with typical relaxor-type relaxation, which makes the system that also orders antiferromagnetically a new multiferroic candidate. We furthermore observe at T_{MI} a sudden occurrence of strong non-equilibrium dynamics of interacting dipolar clusters or domains consistent with a droplet model of spin glasses. The electric field-dependent and slow (glassy) dynamics turns out to be a common theme for a wide class of materials exhibiting electronic ferroelectricity and need to be incorporated in their theoretical description.

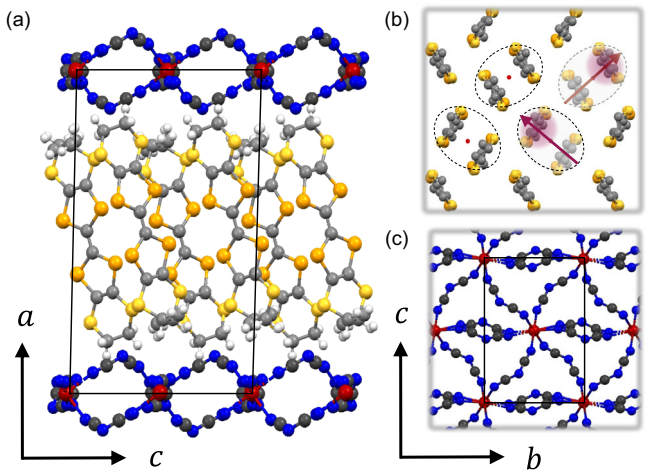

Fig. 1 | Crystal structure of κ-$(BETS)_2Mn[N(CN)_2]_3$. a The conducting BETS layers are separated by insulating $Mn[N(CN)_2]_3$ anion layers. Interlayer direction is the *a*-axis. **b** Projection of the donor and **c** acceptor layer onto the *bc*-plane. In **b** dashed ovals indicate $(BETS)_2$ dimers. For two dimers, the localization of charges on one molecule (red cloud) is indicated by a shift from the center of gravity (red dot) resulting in a quantum electric dipole (red arrow).

Results

The system chosen for our study is κ-$(BETS)_2Mn[N(CN)_2]_3$ (in short κ-BETS-Mn), which recently has attracted interest due to the existence of magnetic Mn^{2+} ions in the acceptor molecules, similar to the compounds λ-$(BETS)_2FeCl_4$ and κ-$(BETS)_2FeBr_4$ exhibiting magnetic-field-induced superconductivity[44,45]. In κ-BETS-Mn, however, specific heat data[46] suggest that the coupling between the BETS spins and the Mn spins is negligible. A rather small coupling constant between the π- and *d*-electrons has been also noted in ref. 47 and was estimated based on Shubnikov-de Haas data[48] to be < 0.12 meV, i.e., more than an order of magnitude lower than for κ-$(BETS)_2FeBr_4$. Based on this finding, theoretical studies including ab initio calculations and modeling of magnetic torque[47] and NMR[49] results identify a spin-vortex crystal order highlighting the importance of magnetic ring exchange[46]. The system remains metallic down to $T_{MI} \sim 20 - 25$ K, where it undergoes a metal-to-insulator (MI) transition due to strong interactions of the charge carriers within the conducting BETS layers. The insulating ground state is sensitive to pressure and can be transformed into a superconducting state with $T_c = 5.7$ K by applying $p = 0.6$ kbar[43], which is similar to the behavior of the Mott insulator κ-$(ET)_2Cu[N(CN)_2]Cl$[50,51]. Band structure calculations[43] reveal a narrow bandwidth and a relatively strong dimerization of the BETS molecules. Quantum oscillations under pressure[48,52] indicate strong electronic correlations suggesting a Mott instability as the origin of the MI transition. Since in the κ-phase dimerized systems, the intra-dimer degrees of freedom and charge-lattice coupling play an important role for the electronic ground state properties[38,53], the system is a good candidate for electronic ferroelectricity.

In order to characterize the transition and study the dynamics related to possible electronic ferroelectricity in single crystals of κ-$(BETS)_2Mn[N(CN)_2]_3$, we performed studies of thermal expansion, resistance fluctuation (noise) spectroscopy and dielectric spectroscopy, see the Methods section below.

Metal-insulator transition

The resistance vs. temperature of two different κ-BETS-Mn samples has been measured perpendicular to the conducting layers upon cooling down the samples with a slow cooling rate of $q \approx -0.7$ K/min. The temperature evolution of the normalized resistance $R(T)/R(300\text{ K})$ is shown in Fig. 2a for samples #1 (in blue) and #2 (in red). At room temperature, the absolute

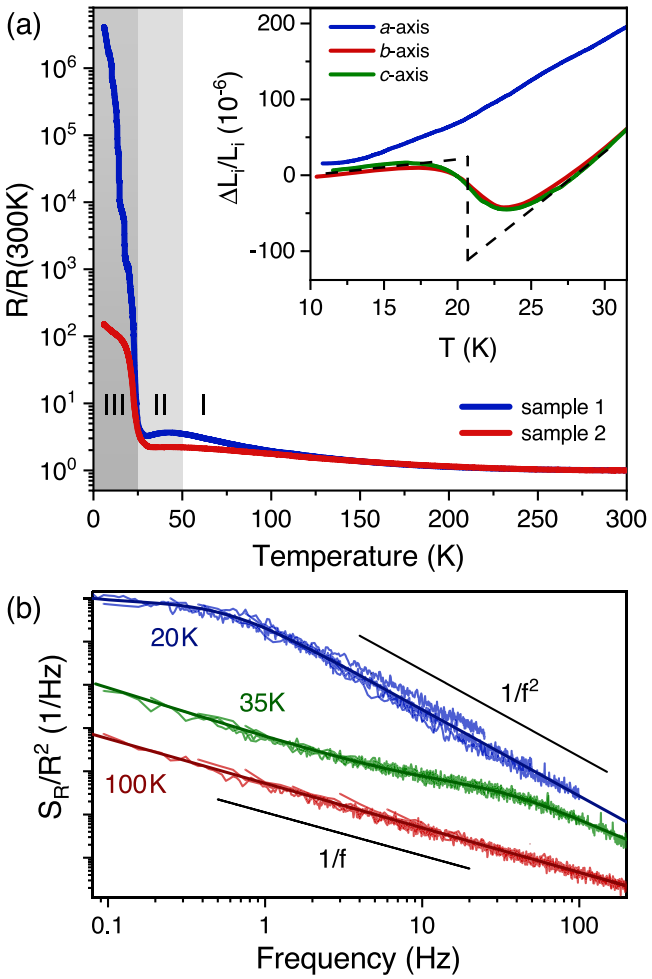

Fig. 2 | Electric, thermodynamic and noise characterization. a Resistance normalized to the value at 300 K vs. temperature of two κ-BETS-Mn samples (#1 in blue, #2 in red). The gray shaded regions correspond to the temperature regimes, where pure $1/f$-type spectra (region I), $1/f$-type and superimposed Lorentzian spectra (region II) and spectra of $1/f^2$-type with a strong time dependence (region III) were observed. The inset shows the relative length change $\Delta L_i/L_i$ vs. T of sample #3 along different in-plane and out-of-plane crystallographic axes around the MI transition. The dashed line illustrates an idealized sharp jump for the in-plane b- and c-axis. **b** Typical fluctuation spectra for regions I, II and III in sample #1. Normalized resistance noise power spectral density, $S_R/R^2(f)$, in a double-logarithmic plot for selected temperatures representing the three temperature regimes. Spectra are shifted for clarity. Different lines shown for each temperature are due to subsequent measurements of different frequency spans. Slopes $S_R/R^2 \propto 1/f$ and $\propto 1/f^2$ are indicated. Solid lines are fits to Eq. (1).

resistance values $R(300\,\mathrm{K})$ of samples #1 and #2 are very similar (977 Ω and 970 Ω) with surface areas $A = 0.24\,\mathrm{mm}^2$, $0.17\,\mathrm{mm}^2$ and crystal thicknesses $d = 55\,\mu$m, $45\,\mu$m, respectively, and both samples show a slight increase in resistance upon cooling from room temperature until a small local maximum is observed at about $T \sim 42$ K. A maximum in $R(T)$ was reported previously[43] at higher temperatures ($T \sim 85$ K), and has been ascribed to the breakdown of transport coherence perpendicular to the conducting layers and strong electron-phonon interactions[42]. The local maximum is also visible in the DC conductivity of our dielectric measurements performed on sample #4, see Fig. S9 in the Supplemental Information (SI), at $T \sim 80$ K in good agreement with ref. 43. Since the sample used for dielectric spectroscopy comes from a different batch, these results emphasize some sample-to-sample dependence of this resistance anomaly.

Below a local minimum at $T \sim 30$ K and 34 K, respectively, the resistance curves for sample #1 and #2 show an abrupt increase by 6 and 2 orders of magnitude, marking the MI transition at $T_{\mathrm{MI}} \approx 22.5$ K defined by a peak in $\mathrm{d}\ln R/\mathrm{d}T$[42] (with the onset of the resistance increase at about 25 K). This coincides with the occurrence of AFM order at $21 - 23$ K in NMR and specific heat measurements[49,53,54]. The drastically different resistance increase at T_{MI} suggests that sample #1 is of better crystal quality. In the insulating regime, the resistance curve of sample #1 shows several jumps, which occurred either spontaneously or are due to nonlinear I-V characteristics, in particular at the lowest temperatures upon reducing the driving current in order to avoid Joule heating. Below $T \sim 20$ K, the strong increase of the resistance flattens, which is more pronounced for sample #2. The white and gray shaded areas in Fig. 2a mark three distinct temperature regimes, where different noise characteristics, i.e., a distinctly different charge dynamics, was observed (see Fig. 2b), which will be discussed in the next section below.

The thermodynamic properties of the MI transition are studied by measuring the thermal expansion of another κ-BETS-Mn sample (#3) from a different batch. The results of the relative length changes $\Delta L_i(T) = L_i(T) - L_i(T_0)$, where T_0 is a reference temperature (typically the base temperature of the experiment), around the MI transition measured along different in-plane and out-of-plane crystallographic axes i are shown in the inset of Fig. 2a. We observe a remarkable anisotropy between the out-of-plane (a) and in-plane (b and c) axes, where only the in-plane axes exhibit a broadened step-like feature at T_{MI}, whereas there are no significant changes in the out-of-plane direction. The slightly lower transition temperature for these measurements may be attributed to varying criteria applied for the characteristic temperature in different physical quantities (the onset temperature is roughly the same), or simply may reflect sample-to-sample differences. The dashed line represents an idealized sharp jump, characteristic for a first-order phase transition, similar to the system κ-$(ET)_2Hg(SCN)_2Cl$, which also exhibits charge ordering and electronic ferroelectricity[28,29,55]. It is worth noting that the jump size of $\Delta L_{b,c}/L_{b,c} \sim 1.3 \times 10^{-4}$ agrees rather well with the volume change calculated by the Clausius-Clapeyron equation using the pressure dependence of T_{MI} reported in ref. 43 and the entropy change ΔS determined in ref. 46.

Charge carrier dynamics

In order to study the charge carrier dynamics around the MI transition at low frequencies, we performed fluctuation spectroscopy measurements in discrete temperature steps using varying setups for different resistance regimes (see "Methods"). Typical spectra for selected temperatures representing three regimes with distinctly different low-frequency dynamics are shown in Fig. 2b. At high temperatures (region I), the resistance noise power spectral density (PSD) shows pure $1/f$-type behavior (red spectrum), i.e., $S_R/R^2 \propto 1/f^{\alpha}$ with the frequency exponent $\alpha = 0.8 - 1.2$. The analysis of these spectra for $T > 50$ K implies enhanced structural dynamics, likely related to the abovementioned peak in the resistivity, and will be published elsewhere. For temperatures below and just above the MI transition, however, a more complex behavior of the charge carrier dynamics emerges. In temperature region II above T_{MI} (light gray shaded area), we observe Lorentzian spectra superimposed on a $1/f$-type 'background' (green), which are caused by dominating two-level fluctuators. At temperatures below T_{MI} (region III, dark gray shaded area), we find strongly enhanced Lorentzians with $S_R/R^2 \propto 1/f^2$ above about $f = 1$ Hz (blue), which are both current dependent and time dependent, see the small offset for subsequent frequency spans for $T = 20$ K in Fig. 2b. This suggests, respectively, (i) a non-linear coupling to the electric field, and (ii) non-equilibrium dynamics and spatial correlations emphasizing the metastable character of the charge carrier dynamics. Therefore, measurements of the so-called 'second spectrum' $S^{(2)}(f_1, f_2)$ (see "Methods") have been performed to further analyze the observed ergodicity breaking, see below. We start, however, by discussing the temperature-dependent 'first spectrum' $S^{(1)}(f, T)$, Fig. 2b, in regime II (considering at first only the $1/f$-type 'background' without the superimposed Lorentzian contribution) and regime III.

Figure 3a shows the spectral weight $\int_{f_{\mathrm{min}}}^{f_{\mathrm{max}}} S_R(f)/R^2 \mathrm{d}f$, which corresponds to the variance of the signal for the given bandwidth, vs.

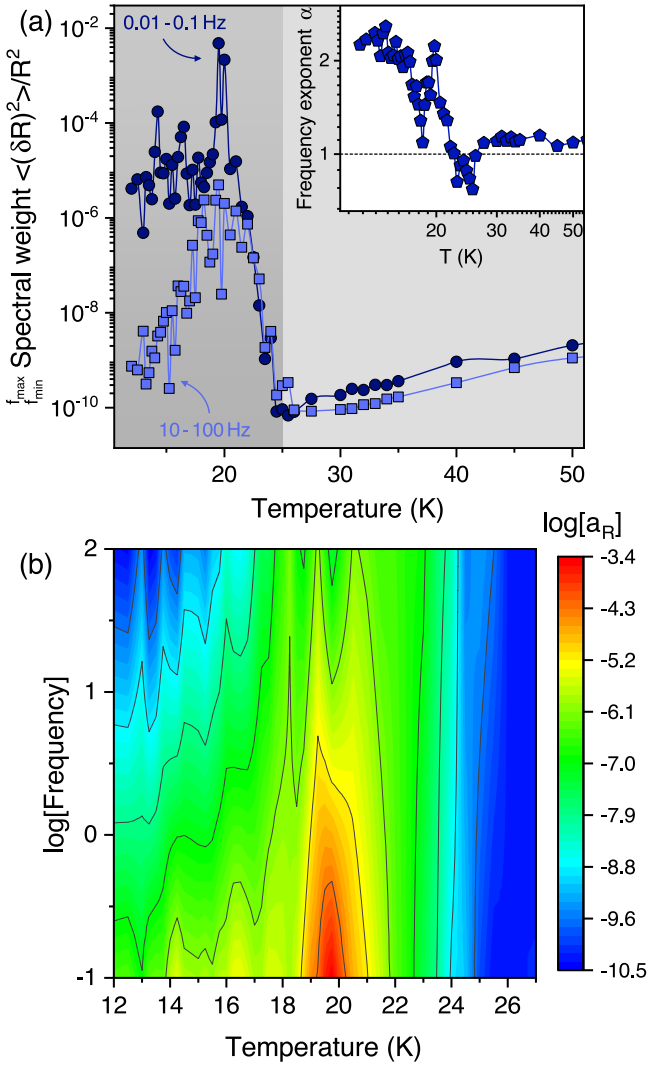

Fig. 3 | Low-frequency charge carrier dynamics. a Spectral weight for different frequency ranges ([0.01, 0.1 Hz] and [10, 100 Hz]) of sample #1 vs. temperature around the MI transition (light gray: regime II and dark gray: III). The inset shows the frequency exponent α vs. logarithmic temperature. **b** Contour plot of the relative noise level $a_R = S_R/R^2 \times f$ in log scale in dependence of temperature and logarithmic frequency.

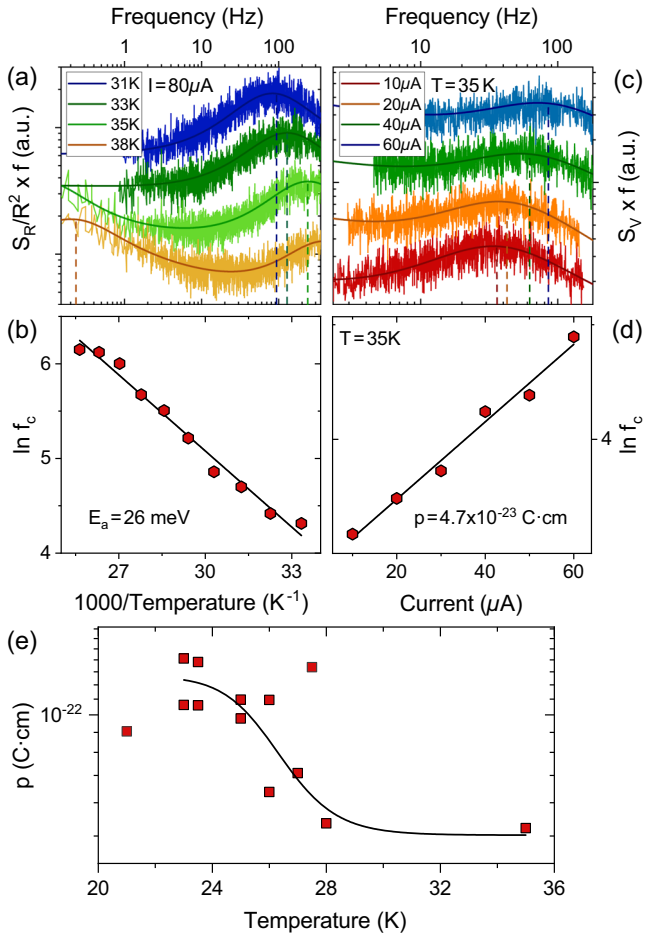

Fig. 4 | Two-level fluctuations. a Lorentzian noise contribution as $S_R/R^2 \times f$ vs. f superimposed on a $1/f$-type 'background' for different temperatures and constant current ($I = 80\ \mu$A) for sample #2. The corresponding shift of the corner frequency given by the maximum of the curves (dashed lines), is shown for the three highest temperatures in **b** vs. the inverse temperature with the slope (black line represents an Arrhenius fit) revealing the activation energy. (Dashed line for the 38 K curve in **a** indicates the presence of a second Lorentzian peak at lower frequencies, see also Fig. S2.) **c** Lorentzian contribution as $S_V \times f$ vs. f for $T = 35$ K and different currents, revealing a shift of the corner frequency as illustrated in **d**. The dipole moment, which is extracted from the slope of the linear fits according to Eq. (2) shown in **d**, is displayed in **e** vs. temperature. The black line is a guide to the eye.

temperature in a certain frequency interval $[f_{\min}, f_{\max}]$ for two frequency bandwidths [0.01, 0.1 Hz] and [10, 100 Hz]. Clearly, at all these frequencies the MI transition is accompanied by a drastic increase of the noise PSD's spectral weight by many orders of magnitude, culminating in a maximum at $T \sim 20$ K, which is more pronounced and sharp for the lower frequency bandwidth [0.01, 0.1 Hz]. A striking observation is that upon further cooling, after a drastic increase by more than seven orders of magnitude, the noise level at these low frequencies saturates at a high level below the peak (about five orders of magnitude higher than at the onset of the transition), whereas the spectral weight for the higher frequency window [10, 100 Hz] decreases upon further cooling to a value comparable to that above the transition. Thus, the charge carrier dynamics below T_{MI} is dominated by rather slow fluctuations. The spectral weight of fluctuations with $S_R \propto 1/f^{\alpha}$ (the noise magnitude) is reflected by the frequency exponent $\alpha(T) = -\partial \ln S_R(T)/\partial \ln f$, shown in the inset of Fig. 3a, where $\alpha = 1$ corresponds to a homogeneous distribution of the energies of fluctuators contributing to the $1/f$-type noise, and $\alpha > 1$ and $\alpha < 1$ correspond to slower and faster fluctuations in comparison, respectively[56]. Upon approaching the MI transition, α being slightly larger than 1 first drops below 1 at about 25 K (onset of MI transition) representing an initially faster dynamics, before it strongly increases to a peak value $\alpha \sim 2$ at 20 K, indicating a strong shift of spectral weight to lower frequencies and a drastic slowing down of the dynamics. Below the peak, the fluctuations seem to become faster again upon further cooling but then saturate at consistently high values. A spectrum with $\alpha = 2$ is a signature of non-equilibrium dynamics and often results from a high-frequency tail of a single Lorentzian (cf. blue curve in Fig. 2b), which dominates the fluctuations over the entire frequency range of our measurements and implies a switching of the system mainly between two subsequent states. The overall picture of an enhanced noise level and drastic slowing down of charge carrier dynamics is highlighted in a contour plot of the so-called relative noise level $a_R = S_R/R^2 \times f$ (see Fig. 3b) vs. temperature and frequency. a_R, a dimensionless quantity characterizing the strength of the fluctuations, upon cooling clearly starts to increase below the onset of the MI transition $T = 25$ K at all frequencies and peaks at about $T = 19 - 20$ K. The noise maximum is more pronounced at lower frequencies (note that a_R and f are shown on a logarithmic scale). In particular, at low temperatures, only the slow fluctuations prevail, whereas at higher frequencies, the noise level of $T > T_{MI}$ is recovered. The noise magnitude for sample #2 (see Fig. S1 in

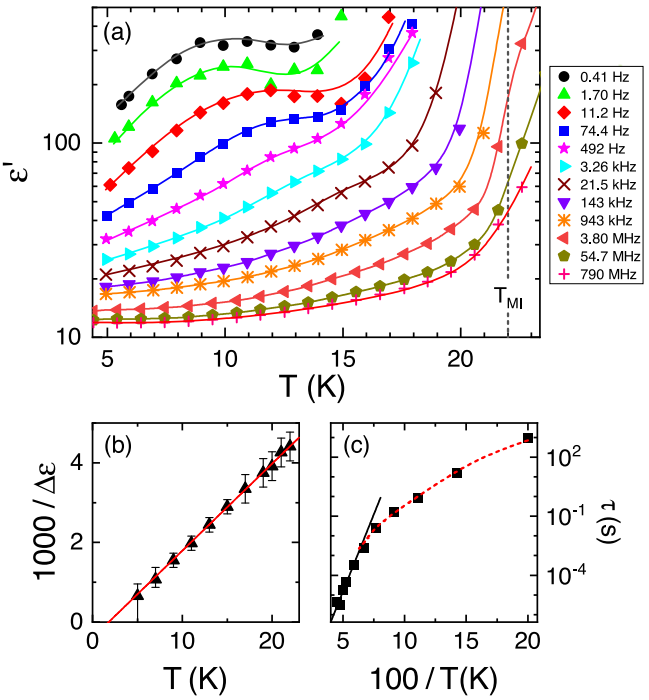

Fig. 5 | Dielectric properties. a Temperature dependence of the dielectric constant measured at various frequencies. The vertical dashed line indicates the onset temperature of the metal-insulator transition which is at 22 K for this sample. The lines are guides for the eye. **b** Inverse relaxation strength of the intrinsic relaxation detected at $T < T_{MI}$ as deduced from fits of the frequency-dependent dielectric data using an equivalent-circuit approach (see SI for details). The line demonstrates Curie-Weiss behavior with $T_{CW} = 1.8$ K. **c** Arrhenius representation of the temperature-dependent relaxation time of the intrinsic relaxation process as obtained from the fits. The solid line is a fit of the data above 15 K by an Arrhenius law with an energy barrier of 31 meV. The dashed line is a guide to the eye.

the SI) yields qualitatively similar results, whereas the noise increase is not as pronounced and not as sharp as for sample #1 analogous to the resistance behavior.

Now we also consider the Lorentzian spectra superimposed on the 1/*f*-type noise and describe the fluctuations by

$$\frac{S_R(f,T)}{R^2} = \frac{a}{f^{\alpha}} + \frac{b}{f^2 + f_c^2} \quad (1)$$

for temperatures from 50 K down to 21 K, i.e., the noise peak below the onset of the MIT (regime II), exemplarily shown in Fig. 4 for sample #2, where $a(T)$ and $b(T)$ are the amplitudes of the 1/*f*-type and Lorentzian noise contributions, with frequency exponent $\alpha(T)$ and corner frequency $f_c(T)$, respectively. Since observed time dependences of the spectra below T_{MI} indicate that the fluctuations are not statistically stationary in regime III, in the following we discuss the observed systematic non-linear current dependence of the spectra only for temperature regime II. By multiplying the noise PSD with frequency, $S_R/R^2 \times f$, the 1/*f*-type contribution becomes a more-or-less constant 'background', thereby emphasizing the Lorentzian contribution with its maximum at the corner frequency f_c. This frequency (marked by dashed lines) shifts as a function of temperature, as shown in Fig. 4a for the corresponding switching process with constant current ($I = 80\,\mu$A). An Arrhenius representation, shown in Fig. 4b, reveals thermally-activated behavior $f_c = f_0 \exp(-E_a/k_B T)$ with an attempt frequency f_0 of order typical phonon frequencies and an activation energy of $E_a = 26$ meV. We note that the curves at 35 K and 38 K in Fig. 4a reveal the presence of a second Lorentzian peak at lower frequeny. Indeed, in addition to the 1/*f* term, two Lorentzian contributions fit the spectra rather well (for 38 K, the low-frequency one is indicated by a vertical dashed line). Correspondingly, different measurement runs (see SI, Fig. S2) during warming and cooling reveal various dominating switching processes depending on the temperature: for $T = 35 - 50$ K we observe two-tevel switching with $E_a = 72 - 86$ meV, whereas for lower temperatures $T = 40 - 25$ K processes with $E_a = 34 - 40$ meV and $E_a = 22 - 26$ meV are found, see SI for details. As discussed in the following, we assign these two-level processes to thermally-activated switching of clusters of quantum electric dipoles fluctuating collectively, i.e., polar nanoregions. A distribution of cluster sizes likely is the reason for the range of activation energies being observed at different temperatures. The origin of these values at constant bias and temperatures above the metal-insulator transition should be related to the incipient localization of charge carriers.

Strikingly, besides the shift with temperature, we observe a strong current dependence of the Lorentzian contribution, see Fig. 4c for another measurement run. At fixed temperature, increasing currents shift the corner frequency to higher values and the magnitude of the Lorentzian $b(T)$ gets suppressed, very similar to previous observations in the square lattice Mott insulator and relaxor ferroelectric β'-$(ET)_2ICl_2$[57]. (Therefore, it is important to note that the temperature-dependent shift discussed above was always analyzed for the maximum applied current.) The linear increase of the corner frequency revealed in a plot of $\ln f_c$ vs. current, see Fig. 4d, indicates that the energy landscape of the thermally activated two-level processes is influenced by the dipole energy $-E_{dipole} = p\mathcal{E}$ according to[57,58]

$$f_c = f_0 \exp\left(\frac{p\mathcal{E} - E_a}{k_B T}\right), \quad (2)$$

where $\mathcal{E}$ denotes the electric field. The dipole moment p at a fixed temperature can be determined from a linear fit of the data shown in Fig. 4d with the slope yielding $p = 4.7 \cdot 10^{-23}$ Ccm at $T = 35$ K, where the electric field is calculated from the applied current, the temperature-dependent resistance and the sample thickness. For κ-$(BETS)_2Mn[N(CN)_2]_3$ very recent vibrational infrared spectroscopy measurements revealed a small but significant charge disproportionation on the dimer which tentatively has been estimated to $\delta \lesssim 0.02 - 0.05e$[59]. This corresponds to a fluctuating nanoscale polar region of radius 3 − 5 nm for spherical PNR or 5 − 8 nm for cylindrical PNR with the height of the unit cell (one molecular layer). This is comparable though somewhat smaller than the PNR size estimated for β'-$(ET)_2ICl_2$ with $\delta \leq 0.1e$[33,57]. The temperature evolution of p is displayed in Fig. 4e and, despite some scattering in the data, reveals increasing values for decreasing temperatures, which appear to saturate below T_{MI}. We note that a qualitatively similar behavior is observed for sample #1 but a clear systematic of the Lorentzian spectra which allowed to track $p(T)$ was only observed for sample #2. We speculate that this might be caused by the higher degree of disorder for the latter sample, which may be favorable for the formation of PNR [36].

Dielectric properties

In order to elucidate the yet unknown electronic state at low temperatures especially with regard to the formation of electronic ferroelectricity, dielectric measurements in a broad frequency range 0.1 Hz < ν < 1.8 GHz were performed at temperatures $T = 5 - 300$ K. This technique is complementary to the resistance noise spectroscopy discussed above in two ways. First, dielectric spectroscopy can capture the dynamics of individual electric dipoles, i.e., on a microscopic level, fluctuating in an ac electric field and it covers a broader frequency range. In contrast, resistance noise spectroscopy captures the dynamics of larger scale polar objects, PNR or domains, the fluctuations of which couple to the resistivity. Second, whereas dielectric spectroscopy requires a sufficiently insulating behavior of the measured sample, resistance noise spectroscopy works for sufficiently conducting samples. Therefore, complementary information on the dynamics of microscopic objects can be gained from the combination of the two spectroscopies.

In the present case, the relatively high conductivity of κ-BETS-Mn above the MI transition leads to pronounced non-intrinsic effects (so-called Maxwell-Wagner relaxations)[60,61], probably due to the formation of

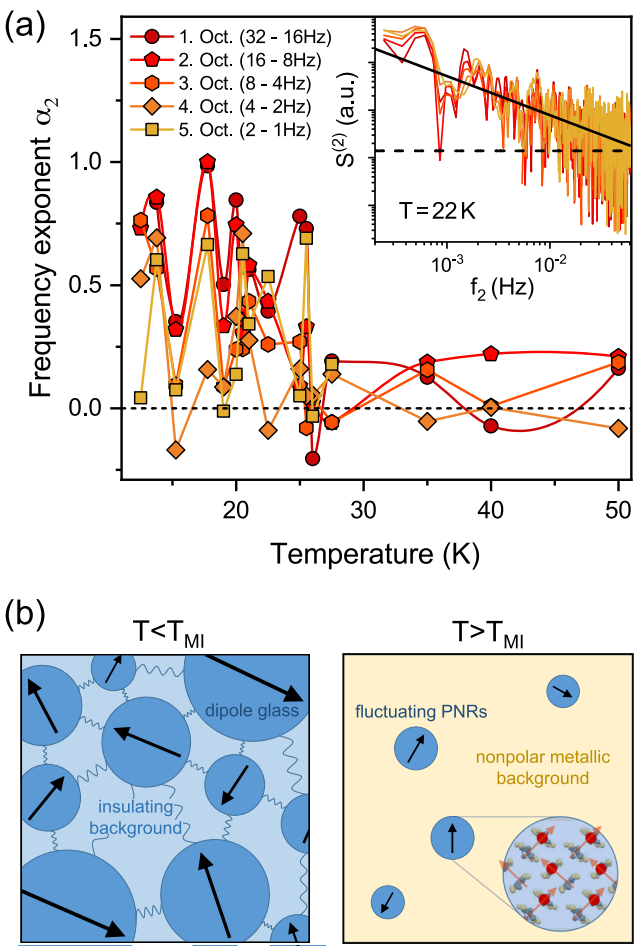

Fig. 6 | Non-equilibrium dynamics and suggested origin. a Frequency exponent α_2 of the second spectrum $S^{(2)} \propto 1/f_2^{\alpha_2}$ against temperature, which is extracted from a linear fit of the PSD in a double logarithmic plot, as shown in the inset. Different red to orange colors mark different octaves. **b** Schematic illustration of the dipolar dynamics that leads to the observed behavior in the resistance noise and dielectric properties. Left: Frozen dipole-glass state below T_{MI} exhibiting relaxor-type ferroelectricity and strong non-equilibrium dynamics. Right: Polar nanoregions (PNR) performed in the metallic phase above T_{MI}. Whereas above T_{MI}, the PNR are independently fluctuating, they exhibit spatial correlations in the insulating/ferroelectric regime (indicated by wavy lines).

Schottky diodes at the interfaces between sample and metallic electrodes (see SI for a detailed discussion). Figure 5a, showing the temperature dependence of the dielectric constant ε' at selected frequencies, is thus restricted to temperatures $T \lesssim T_{MI}$. The strong increase of ε' at high temperatures is due to the onset of the mentioned Maxwell-Wagner relaxations. At lower temperatures, however, indications for an intrinsic relaxation process are observed, signified by a sigmoidal curve shape, shifting to lower temperatures with decreasing frequency. At the lowest frequencies, a peak develops and ε' reaches relatively high values of several hundred. Neglecting the non-intrinsic high-temperature increase, the overall behavior in Fig. 5a is that of the typical dielectric response of relaxor ferroelectrics[62,63]. This makes κ-$(BETS)_2Mn[N(CN)_2]_3$ most likely another example of an organic multiferroic compound. (By the current definition of multiferroicity as a coexistence of ferroelectric and ferro-, ferri- or antiferromagnetic order the multiferroic material is denoted as type I if the magnetic and ferroelectric orders occur independently. If the ferroelectric and magnetic transitions emerge jointly, the multiferroic is of type II[12]. Regarding a possible magnetoelectric coupling, the magnetic vortex crystal order that has been suggested for κ-BETS-Mn[46] is ultimately odd under time reversal and even under spatial inversion, so it has similar symmetry properties as in the antiferromagnetic order in κ-$(ET)_2Cu[N(CN)_2]Cl$. Symmetry disallows linear coupling to a ferroelectric order parameter, but quadratic coupling is allowed.)

As mentioned above, relaxor ferroelectricity, believed to arise from a cluster-like, short-range ferroelectric order[36,37,64], was also observed in several other charge-transfer salts[26,31,33,34,39,65,66]. The intrinsic nature of the relaxor-like low-temperature behavior is strongly supported by the similarity of the results obtained using a different experimental setup, different samples and contact materials as discussed in the SI (Figs. S5 and S6). To further corroborate the relaxor ferroelectricity in κ-BETS-Mn, polarization measurements as provided, e.g., in ref. 34,65,67 would be desirable. Unfortunately, the rather high conductivity of this material[42,43] makes such measurements impracticable. We therefore refer to our system as a multiferroic candidate.

Fits of the dielectric spectra, using an equivalent-circuit approach to account for the non-intrinsic contributions, allows deducing the relaxation strength $\Delta\varepsilon$ and the relaxation time τ of the intrinsic low-temperature relaxation (see SI for a detailed discussion). Figure 5b shows the inverse of the resulting $\Delta\varepsilon(T)$. The observed linear increase indicates a Curie-Weiss behavior, $\Delta\varepsilon \propto 1/(T - T_{CW})$ with $T_{CW} = 1.8$ K. T_{CW} represents an estimate of the quasistatic dipolar freezing temperature. It is even lower than the already rather low $T_{CW} = 6$ K of κ-$(ET)_2Cu_2(CN)_3$[39] and much lower than in other charge-transfer-salt relaxors where T_{CW} values between 35 and 206 K were reported[33,34,65,66].

Figure 5c shows an Arrhenius plot of the temperature dependence of the relaxation time as derived from the fits. The observed non-linear behavior clearly evidences deviations from simple thermal activation of the detected dipolar dynamics which at best holds for $T > 15$ K only (solid line). In relaxor ferroelectrics, $\tau(T)$ often can be described by the Vogel-Fulcher-Tammann law, which indicates glassy freezing of the dipolar dynamics at low temperatures[64]. However, in the Arrhenius representation of Fig. 5c, this should lead to an increase of slope with decreasing temperature. Instead, we observe a successively weaker temperature dependence of τ at low temperatures (dashed line in Fig. 5c). This finding can be explained by a crossover from thermally-activated behavior to quantum-mechanical tunneling below about 15 K: as the tunneling probability should be essentially temperature independent, a weaker temperature dependence of τ arises when, upon cooling, thermal activation becomes increasingly unlikely and tunneling phenomena start to dominate. We note that a similar unusual temperature dependence of the relaxation in glassy systems has also been found in a theoretical study of a 2D doped classical antiferromagnet, where slow and spatially heterogeneous dynamics occurs, and the relaxation times associated with spin correlations and diffusion of particles both diverge at low temperatures in a sub-Arrhenius fashion[68].

We emphasize again that the relaxational processes observed by resistance fluctuation and dielectric spectroscopy, even though the frequency (and temperature) ranges overlap, are attributed to different microscopic processes. The former is connected to the switching of PNR associated with relatively large effective energy barriers, thus resulting in rather slow dynamics. The latter captures much faster processes, pointing to reorientational dynamics that occurs on a smaller length scale than the switching of the whole PNRs. Interestingly, in the theoretical treatment of relaxor ferroelectrics by Vugmeister[69] the presence of local polarization dynamics *inside* the PNRs was assumed. An alternative mechanism for faster dynamics in relaxors is the motion of the PNR boundaries as considered in the breathing model by Glazounov and Tagantsev[70]. In combination, the complementary methods provide a more complete picture of the relaxation dynamics in electronic ferroelectrics where disorder and/or competing interactions lead to emergent electronic phase separation. Importantly, the PNR form as fluctuating units that can be stabilized in an electric field already above the MI transition and therefore are precursors of the relaxor-type ferroelectricity observed below T_{MI}.

Nonequilibrium dynamics

The results of the dielectric spectroscopy confirm the slowing down of dipolar motion and local ferroelectric correlations for decreasing temperatures,

typical for relaxor materials. We now discuss another characteristic feature below the MI transition, i.e., a sudden onset of a strong time dependence of the resistance/conductance noise PSD in the insulating state below T_{MI}, which results in variations of the spectral weight for repeated measurements at the same temperature, i.e., the fluctuations are not statistically stationary anymore. A similar behavior has been observed for samples #1 and #2, whereas for sample #1, the noise level varies with time by up to one order of magnitude (cf. Fig. S3a in the SI), while for sample #2 the changes are less pronounced. This so-called spectral wandering should be reflected by a non-Gaussian probability distribution of the time signal, which is often caused by spatially correlated fluctuators[71–75]. Indeed, below T_{MI}, we observe deviations from a Gaussian distribution, see Fig. S3c in the SI, very similar to the dynamics of the first-order electronic phase transition in complex transition metal oxides[76], which was ascribed to electronic phase separation. In order to identify interacting/spatially-correlated fluctuators, we investigated the higher-order correlation function by measurements of the second spectrum $S^{(2)}(f_2, f_1, T)$, which corresponds to the PSD of the fluctuating first spectrum (see e.g., refs. 77–79 for more detailed information). Here, $f_1 \equiv f$ and f_2 correspond to frequencies of the first and second spectrum, respectively, where f_2 results from the time dependence of $S(f, T) \equiv S^{(1)}(f_1, t)$ at fixed frequency f_1. In the case of correlated fluctuators, the second spectrum often shows a frequency dependence according to $S^{(2)} \propto 1/f_2^{\alpha_2}$ with $\alpha_2 > 0$, whereas $\alpha_2 = 0$ for statistically stationary, Gaussian fluctuations[80].

A typical spectrum of $S^{(2)}(f_2)$ is displayed in the inset of Fig. 6a for sample #1 at $T = 22$ K and indeed reveals a $S^{(2)} \propto 1/f_2$ behavior (black line). The time-dependent spectral weight of the first spectrum, which is used to calculate the second spectrum, is exemplarily shown in the SI [Fig. S3b]. The second spectrum is usually analyzed for different octaves, which are indicated by red to orange colors in Fig. 6a and correspond to varying frequency ranges of the first spectrum (see Fig. S3a in the SI). In order to investigate the development of spatial correlations when crossing the MI transition, we analyzed the frequency exponent α_2 of the second spectrum over a wide temperature range, see Fig. 6a. Whereas above the MI transition $S^{(2)}$ is roughly frequency independent ($\alpha_2 \sim 0$), there is a sudden increase of the frequency exponent up to $\alpha_2 \sim 1$ below T_{MI}, coinciding with the strong increase in the magnitude of slow fluctuations $S^{(1)}(f_1)$ shown in Fig. 3 above. Clearly, the MI transition is accompanied by strong non-equilibrium charge dynamics indicative of spatially-correlated fluctuators and a dipolar glass.

Discussion

We put the results on κ-$(BETS)_2Mn[N(CN)_2]_3$ in context to other organic charge-transfer salts. Prominent examples are the Mott insulators κ-$(ET)_2Cu[N(CN)_2]Cl$, where order-disorder-type electronic ferroelectricity emerges within a Mott insulating phase[15], whereas it coincides with a Mott metal-insulator transition in κ-$(ET)_2Hg(SCN)_2Cl$[28–30]. Interestingly, in the former system both long-range order or relaxor-type ferroelectricity can arise[15,31]. The latter behavior, indicative of interacting electric dipoles in the presence of a random potential or competing interactions, is more abundant and has been observed first in the system κ-$(ET)_2Cu_2(CN)_3$[39]. Likewise, relaxor-type ferroelectricity occurs in other κ-$(ET)_2X$ compounds, as e.g., X = $Ag_2(CN)_3$, as well as in systems with other packing motifs or donor molecules, e.g., β'-$(ET)_2ICl_2$, α-$(ET)_2I_3$ and various $Pd(dmit)_2$ systems[32–35]. For κ-$(ET)_2Hg(SCN)_2Br$, a quantum dipole liquid has been suggested[81] in which electric dipoles created by intradimer charge imbalance remain fluctuating down to low temperatures. Interestingly, for this compound inhomogeneity, local correlation, and slow dynamics indicative of spatial correlations on the nanometer length scale has been reported for the spin degrees of freedom forming clusters emerging in the electric-dipole liquid[82].

For the present κ-$(BETS)_2Mn[N(CN)_2]_3$, the following tentative scenario for the dynamics of the electric dipoles residing on the $(BETS)_2$ dimers is suggested from dielectric spectroscopy. Upon approaching T_{MI} from above, due to strong electron correlations the π-holes become localized on the dimers driving the system into the Mott insulating state going along with a strong increase in both resistance and resistance noise. However, the holes remain delocalized on their respective dimers and the hopping of the holes between the two molecules corresponds to the reorientation of an associated dipolar moment, detected by dielectric spectroscopy.

With decreasing temperature, this local motion starts to slow down and, simultaneously, local ferroelectric correlations—which, however, partly have been developed already above T_{MI}—lead to the cluster-like ferroelectric order, typical for relaxor ferroelectrics. Upon cooling through the MI transition, those PNR which dominate the resistance noise and preexist as fluctuating entities above T_{MI} undergo a transition of interacting two-level systems. The abrupt and drastic change of the statistical properties of the fluctuations and onset of non-equilibrium dynamics—a signature of spatial correlations[71–75]—right at the onset of the metal-insulator transition can be explained by a change of the background matrix, which is metallic above T_{MI} providing screening of the dipole moments. Below T_{MI}, the insulating background allows the PNR to interact, see Fig. 6b for a schematic illustration. Here, it is important to note that, as described in the Methods section below, the interlayer charge transport shares the features of the in-plane carrier dynamics.

The strong enhancement of the noise magnitude S_R/R^2 at the MI transition at low frequencies below ~1 kHz shown in Fig. 3 for sample #1 can be considered a signature of the first-order phase transition accompanied by emergent electronic phase separation[76,83,84]. The enhancement of the frequency exponent α corresponding to a drastic shift of spectral weight to low frequencies and slowing down of charge carrier dynamics which persists at low temperatures, is consistent with the localization of charge carriers and the onset of the freezing of PNR switching. The more inhomogeneous transition in the resistivity observed for sample #2 results in a broadened feature also in the noise magnitude since disorder may lead to the localization of charge carriers in different parts of the sample at slightly different temperatures.

Moreover, whereas in conventional relaxors the correlated dipolar dynamics arise from ionic motions and exhibit glass-like freezing upon further cooling[62–64], in κ-BETS-Mn tunneling starts to dominate at low temperatures, preventing the further slowing down and final arrest of the essentially electronic dynamics. This may explain the saturation of the noise level/persistence of slow dynamics at low frequencies and low temperatures. We note that other, more complex scenarios, for example interfacial charge defects within a domain structure arising from coupling of the organic layers to the anion network have been discussed in ref. 85 in order to explain the relaxor dynamics in κ-$(ET)_2Cu_2(CN)_3$. For the present system, however, the existence of PNR and non-equilibrium dynamics is evident.

Finally, in analogy to spin glasses, the origin of correlated fluctuating PNR may be classified by the frequency dependence of $S^{(2)}$ vs. f_2/f_1 in the hierarchical (replica symmetry breaking) or droplet model[72,77,86–88]. The models can be distinguished by their scaling properties, where in a plot $\log S^{(2)}(f_2, f_1)$ vs. $\log(f_2/f_1)$ all curves collaps in the picture of spectral wandering between metastable states related by a kinetic hierarchy. Such a behavior we only observe in close vicinity to T_{MI} (see SI, Fig. S4). In contrast, for all investigated temperatures $T < T_{MI}$ the curves for different octaves are clearly shifted in accordance with a droplet model indicating interacting clusters with a characteristic size distribution, where smaller droplets occur more frequently than large droplets which in turn are more likely to interact. It is tempting to identify these droplets with the (possibly merged) PNR. The variation with different octaves is refelected in long-time measurements of the spectral weight of the first spectrum, where fluctuating processes with time constants of a few hours were observed. This indicates that the noise level switches between a few states only, whose transition times sometimes exceed the measuring time, resulting in different α_2 values for repeated measurement runs. Such behavior was also observed in the dielectric polarization noise of a glassy system[89] where the spectra continued to change even after several hours due to the large heterogeneity of time constants, which, in general, is a prominent feature of glassy dynamics. It should be noted that in canonical glass forming systems, non-equlibrium dynamics is expected below the glass-transition temperature T_g only. In the present case, the onset of such effects just below T_{MI} shown in Fig. 6a points to $T_g \approx T_{MI}$. Having in mind the commonly-used relation $\tau(T_g) \approx 100$ s[90], the relaxation

time of the PNRs then should approach a value of 100 s for $T \rightarrow T_{MI}$. This seems to contradict the Arrhenius law employed to fit the peak frequencies in Fig. 4b, whose extrapolation leads to $T_g \approx 15$ K (using $\tau = 1/(2\pi f_c)$). This apparent discrepancy may well point to non-Arrhenius temperature dependence of $\tau(T)$, which is typical for glass forming systems[90]. In Fig. 4b, it should lead to deviations from linear behavior, which, however, are not detectable due to the rather restricted temperature and frequency window of the observed fluctuations. Importantly, there are strong non-equilibrium dynamics for temperatures less than T_{MI}, whether or not this temperature coincides with a "true" glass transition.

To summarize, our results emphasize the importance of intra-dimer charge degrees of freedom resulting in electronic ferroelectricity in dimerized ET- and BETS-based organic conductors, and demonstrate that the combination of fluctuation and dielectric spectroscopy is a powerful tool to study dipolar dynamics in these systems in different time and length scales. We have identified fluctuating polar nanoregions (PNR) as precursors of a relaxor ferroelectric state and identified κ-$(BETS)_2Mn[N(CN)_2]_3$ as a possible new multiferroic material. Upon cooling through the metal-insulator transition, non-equilibrium dynamics of interacting PNR emerges consistent with a glassy droplet model. Slow dynamics that depends strongly on temperature and the applied electric field should be considered in future theoretical descriptions since it appears to be a common theme for a number of different organic dimer Mott insulator compounds where electronic ferroelectricity is discussed, among them κ-$(ET)_2Cu[N(CN)_2]Cl$, $\beta\prime$-$(ET)_2ICl_2$, κ-$(ET)_2Hg(SCN)_2Cl$ or κ-$(ET)_2Cu_2(CN)_3$, where charge order within the dimers results in an electric polarization. Interestingly, terahertz-field-induced polar charge order for κ-$(ET)_2Cu[N(CN)_2]Cl$ suggests the coupling of charge and spin degrees of freedom to play an important role in the stabilization of the polar charge order as well as the intermolecular Coulomb interaction and the electron-lattice interaction[23]. It is worth further investigating the influence of competing interactions and a random lattice potential, that may cause the glassy/relaxor properties, and—in view of searching candidates for organic spintronics applications, considering the peculiar spin-vortex crystal order in κ-$(BETS)_2Mn[N(CN)_2]_3$ recently suggested in ref. 46—the coupling strengths between charge, spin and lattice degrees of freedom.

Methods

Samples investigated

Single crystals of κ-BETS-Mn with plate-like geometry were grown by electrochemical crystallization[42]. In total five different samples (two for noise spectroscopy, one for thermal expansion measurements and two for dielectric spectroscopy) from three different batches were studied. The samples for dielectric measurements (#4 and #5) and thermal expansion (#3) are from the same batch (Garching-SW-03). The samples for noise spectroscopy are from different batches (sample #1 from batch NKG279 and sample #2 from AD1).

Resistance measurements and fluctuation (noise) spectroscopy

In the present highly anisotropic layered compound the out-of-plane resistance can be most reliably measured, whereas the in-plane resistance suffers from significant parasitic contributions of interplane voltage, (see ref. 91) for a detailed discussion. We therefore focus on the interlayer charge transport and dielectric spectroscopy in the out-of-plane direction. In the present compound, the interlayer transfer energy is much lower than the Fermi energy[91]. Therefore, despite the weak coupling between the layers, the interlayer charge transport at low temperatures and for high-quality samples is dominated by the coherent conduction channel and we can expect that the interlayer transport shares the features of the in-pane carrier dynamics, scaled by the effective mass ratio.

For resistance and noise measurements, 20 μm-thick Pt wires were attached to the largest surface of the samples, corresponding to the conducting *bc*-plane, by using carbon paste. Two contacts on each side of the sample allowed a four-point measurement perpendicular to the BETS layers. The resistance in the metallic region was measured by an AC technique with a lock-in amplifier (Stanford Research 830), whereas below the MI transition a DC configuration with a Keithley Sourcemeter 2612 was used.

The noise power spectral density (PSD) of the resistance fluctuations $\delta R(t) = R(t) - \langle R(t)\rangle$, where $\langle R(t)\rangle$ is the time-averaged mean value that may be considered equal to zero, is defined as:

$$S_R(f) = 2 \lim_{T\to\infty} \frac{1}{T} \left| \int_{-T/2}^{T/2} \delta R(t) e^{-i2\pi ft} dt \right|^2, \quad (3)$$

where the variance of the signal $\langle \delta R(t)^2 \rangle$ is normalized by $\langle \delta R(t)^2 \rangle = \int_0^\infty S_R(f) df$. The Wiener-Khintchine theorem connects the power spectrum of any fluctuating quantity x to a time-like property of the statistically varying function $\delta x(t)$. This time-like property is given by the system's autocorrelation function $\Psi_{xx}(\tau) = \langle x(t) \cdot x(t+\tau)\rangle$ describing the microscopic kinetics of the fluctuation process:

$$S_x(f) = 4 \int_0^\infty \Psi_{xx}(\tau) \cos(2\pi f\tau) d\tau. \quad (4)$$

The Fourier transform can be inverted, i.e., measuring the noise PSD in principle allows access to the correlation function $\Psi_{xx}(\tau)$ which is a non-random characteristic of the kinetics of the system's random fluctuations, describing how the fluctuations evolve in time on average[56,92]. Fluctuation spectroscopy measurements were performed with a four-point AC ($T > T_{MI}$) and four-point DC method ($T < T_{MI}$) by using a preamplifier (Stanford Research 560) and a signal analyzer (Stanford Research 785) (see ref. 56,93 for more detailed information), which provides the power spectral density of the voltage fluctuations by computing the Fast Fourier Transform. For measurements of the second spectrum, we employed a fast data acquisition card (DAQ) (National Instruments PCI-6281) instead of the signal analyzer in order to determine the power spectral densities from the recorded time signal by a software. In many conducting systems (like the present one) the measured spectral density of the noise above the equilibrium one increases with the current I as I^2 (or with the voltage V as V^2). This is usually interpreted as the modulation noise caused by fluctuations (random modulation) of the sample's resistance $\delta R(t)$. According to Kirchhoff's law, the spectral densities of current noise at fixed voltage and voltage noise at fixed current are simply given by $(S_I/I^2)_V = \text{const.} = (S_V/V^2)_I = \text{const.} = S_R/R^2$ where R is the differential resistance[92]. Thus, it is common to consider the resistance or conductance noise power spectral density normalized to the resistance or conductance squared in order to address the relative change in the fluctuation properties.

Capacitive dilatometry

Thermal expansion measurements were performed using a homemade capacitive dilatometer with a maximum resolution of $\Delta L/L \geq 10^{-10}$ based on the model of ref. 94. The quantity of the relative length change $\Delta L_i(T)/L_i$, with $i = a, b, c$, were determined by $\Delta L_i(T) = L_i(T) - L_i(T_0)$ and the starting temperature T_0 of the experiment.

Dielectric spectroscopy

For the dielectric measurements, gold contacts were thermally evaporated on opposite sides of the plate-like crystals, leading to an electrical-field direction perpendicular to the conducting BETS layers. At frequencies $\nu \lesssim 2$ MHz, the dielectric constant ε', the dielectric loss ε'', and the real part of the conductivity σ' were measured using a frequency-response analyzer (Novocontrol Alpha Analyzer). At higher frequencies, a coaxial reflection technique was used[95] employing a Keysight E4991B impedance analyzer. Temperature-dependent measurements down to ~ 5 K were performed using a ^{4}He-bath cryostat (Cryovac). We note that permanent polarization measurements are impractibale due to the large residual conductivity of the samples. Only for resistances above ~ 100 MΩ electrical breakdowns and

trivial conductivity contributions to the polarization are avoided and sufficiently high electric fields can be built up to enable such measurements.

Data availability

All data are available in the main text or the supplementary materials.

Received: 4 December 2023; Accepted: 26 March 2024;
Published online: 28 June 2024

References

1. Sun, D., Ehrenfreund, E. & Vardeny, Z. V. The first decade of organic spintronics research. *Chem. Commun.* **50**, 1781 (2014).
2. Sun, D. et al. Inverse spin Hall effect from pulsed spin current in organic semiconductors with tunable spin-orbit coupling. *Nat. Mater.* **15**, 863 (2016).
3. Dediu, V. A., Hueso, L. E., Bergenti, I. & Taliani, C. Spin routes in organic semiconductors. *Nat. Mater.* **8**, 707 (2009).
4. Dediu, V., Murgia, M., Matacotta, F. C., Taliani, C. & Barbanera, S. Room temperature spin polarized injection in organic semiconductor. *Solid State Commun.* **122**, 181–184 (2002).
5. Xiong, Z. H., Wu, D., Valy Vardeny, Z. & Shi, J. Giant magnetoresistance in organic spin-valves. *Nature* **427**, 821–824 (2004).
6. Grünewald, R. Göckeritz, M., Homonnay, N., Würthner, F., Molenkamp, L. W. & Schmidt, G. Vertical organic spin valves in perpendicular magnetic fields. *Phys. Rev.* **88**, 085319 (2013).
7. Kamiya, T., Kawasugi, Y., Ara, M. & Tada, H. Nonlocal magnetoresistance measurements of the organic zero-gap conductor α-(BEDT-TTF)$_2$I$_3$. *Phys. Rev. B* **95**, 085307 (2017).
8. Naka, M. et al. Spin current generation in organic antiferromagnets. *Nat. Commun.* **10**, 4305 (2019).
9. Qiu, Z., Uruichi, M., Hou, D., Uchida, K., Yamamoto, H. M. & Saitoh, E. Spin-current injection and detection in κ-(BEDT-TTF)$_2$Cu[N(CN)$_2$]Br. *AIP Adv.* **5**, 057167 (2015).
10. Nakajima, R. et al. Giant spin polarization and a pair of antiparallel spins in a chiral superconductor. *Nature* **613**, 497–484 (2023).
11. Eerenstein, W., Mathur, N. D. & Scott, J. F. Multiferroic and magnetoelectric materials. *Nature* **442**, 759–765 (2006).
12. Fiebig, M., Lottermoser, T., Meier, D. & Trassin, M. The evolution of multiferroics. *Nat. Rev. Mater.* **1**, 16046 (2016).
13. Krohns, S. & Lunkenheimer, P. Ferroelectric polarization in multiferroics. *Phys. Sci. Rev.* **4**, 20190015 (2019).
14. Parsonnet, E. et al. Nonvolatile electric field control of thermal magnons in the absence of an applied magnetic field. *Phys. Rev. Lett.* **129**, 087601 (2022).
15. Lunkenheimer, P. et al. Multiferroicity in an organic charge-transfer salt that is suggestive of electric-dipole-driven magnetism. *Nat. Mater.* **11**, 755 (2012).
16. van den Brink, J. & I. Khomskii, D. Multiferroicity due to charge ordering. *J. Phys. Condens. Matter* **20**, 434217 (2008).
17. Horiuchi, S. & Tokura, Y. Organic ferroelectrics. *Nat. Mater.* **7**, 357–366 (2008).
18. Ishihara, S. Electronic ferroelectricity and frustration. *J. Phys. Soc. Jpn* **79**, 011010 (2010).
19. Kimura, T. et al. Magnetic control of ferroelectric polarization. *Nature* **426**, 55–58 (2003).
20. Ikeda, N. et al. Ferroelectricity from iron valence ordering in the charge-frustrated system lufe2o4. *Nature* **436**, 1136–1138 (2005).
21. Fujiwara, K. et al. Direct evidence of electronic ferroelectricity in $YbFe_2O_4$ using neutron diffraction and nonlinear spectroscopy. *Sci. Rep.* **11**, 4277 (2021).
22. Kaneko, T., Sun, Z., Murakami, Y., Golež, D. & J. Millis, A. Bulk photovoltaic effect driven by collective excitations in a correlated insulator. *Phys. Rev. Lett.* **127**, 127402 (2021).
23. Yamakawa, H. et al. Terahertz-field-induced polar charge order in electronic-type dielectrics. *Nat. Commun.* **12**, 953 (2021).
24. Naka, M. & Ishihara, S. Electronic ferroelectricity in a Dimer Mott insulator. *J. Phys. Soc. Jpn* **79**, 063707 (2010).
25. Ishihara, S. Electronic ferroelectricity in molecular organic crystals. *J. Phys. Condens. Matter* **26**, 493201 (2014).
26. Lunkenheimer, P. & Loidl, A. Dielectric spectroscopy on organic charge-transfer salts. *J. Phys. Condens. Matter* **27**, 373001 (2015).
27. Tomić, S. & Dressel, M. Ferroelectricity in molecular solids: a review of electrodynamic properties. *Rep. Prog. Phys.* **78**, 096501 (2015).
28. Drichko, N. et al. Metallic state and charge-order metal-insulator transition in the quasi-two-dimensional conductor κ-(BEDT-TTF)$_2$Hg(SCN)$_2$Cl. *Phys. Rev. B* **89**, 075133 (2014).
29. Gati, E. et al. Evidence for electronically driven ferroelectricity in a strongly correlated dimerized BEDT-TTF molecular conductor. *Phys. Rev. Lett.* **120**, 247601 (2018).
30. Gati, E. et al. Insights from experiment and ab initio calculations into the glasslike transition in the molecular conductor κ-(BEDT-TTF)$_2$Hg(SCN)$_2$Cl. *Phys. Rev. B* **97**, 075115 (2018).
31. Lang, M. et al. Multiferroicity in the mott insulating charge-transfer salt κ-(BEDT-TTF)$_2$Cu[N(CN)$_2$]Cl. *IEEE Trans. Magn.* **50**, 1–7 (2014).
32. Pinterić, M. et al. Anion effects on electronic structure and electrodynamic properties of the Mott insulator κ-(BEDT-TTF)$_2$Ag$_2$(CN)$_3$. *Phys. Rev. B* **94**, 161105 (2016).
33. Iguchi, S. et al. Relaxor ferroelectricity induced by electron correlations in a molecular dimer Mott insulator. *Phys. Rev. B* **87**, 075107 (2013).
34. Lunkenheimer, P. et al. Ferroelectric properties of charge-ordered α-(BEDT-TTF)$_2$I$_3$. *Phys. Rev. B* **91**, 245132 (2015).
35. Abdel-Jawad, M.Tajima, N.Kato, R. & Terasaki, I. Disordered conduction in single-crystalline dimer Mott compounds. *Phys. Rev. B* **88** (2013).
36. Bokov, A. A. & G. Ye, Z. Recent progress in relaxor ferroelectrics with perovskite structure. *J. Mater. Sci.* **41**, 31–52 (2006).
37. Fu, D. et al. Relaxor Pb($Mg_{1/3}Nb_{2/3}$)O_3: a ferroelectric with multiple inhomogeneities. *Phys. Rev. Lett.* **103**, 207601 (2009).
38. Hotta, C. Quantum electric dipoles in spin-liquid dimer Mott insulator κ-(ET)$_2$Cu$_2$(CN)$_3$. *Phys. Rev. B* **82**, 241104 (2010).
39. Abdel-Jawad, M. et al. Anomalous dielectric response in the dimer Mott insulator κ-(BEDT-TTF)$_2$Cu$_2$(CN)$_3$. *Phys. Rev. B* **82**, 125119 (2010).
40. Deglint, M. B., Akella, K. & P. Kennett, M. Charge glass in an extended dimer Hubbard model. *Phys. Rev. B* **106**, 085123 (2022).
41. Hotta, C., Yoshida, T. & Harada, K. Quantum critical dynamics in the two-dimensional transverse ising model. *Phys. Rev. Res.* **5**, 013186 (2023).
42. Kushch, N. D. et al. π-Donor BETS based bifunctional superconductor with polymeric dicyanamidomanganate(II) Anion Layer: κ-(BETS)$_2$Mn[N(CN)$_2$]$_3$. *J. Am. Chem. Soc.* **130**, 7238–7240 (2008).
43. Zverev, V. N. et al. Temperature-pressure phase diagram and electronic properties of the organic metal κ-(BETS)$_2$Mn[N(CN)$_2$]$_3$. *Phys. Rev. B* **82**, 155123 (2010).
44. Uji, S. et al. Magnetic-field-induced superconductivity in a two-dimensional organic conductor. *Nature* **410**, 908–910 (2001).
45. Fujiwara, H., Kobayashi, H., Fujiwara, E. & Kobayashi, A. An indication of magnetic-field-induced superconductivity in a bifunctional layered organic conductor, κ-(BETS)$_2$FeBr$_4$. *J. Am. Chem. Soc.* **124**, 6816–6817 (2002).
46. Riedl, K. et al. Spin vortex crystal order in organic triangular lattice compound. *Phys. Rev. Lett.* **127**, 147204 (2021).
47. Vyaselev, O. M., Biberacher, W., Kushch, N. D. & Kartsovnik, M. V. Interplay between the *d*- and π-electron systems in magnetic torque of the layered organic conductor κ-(BETS)$_2$Mn[N(CN)$_2$]$_3$. *Phys. Rev. B* **96**, 205154 (2017).

48. Kartsovnik, M. V. et al. Shubnikov-de Haas oscillations and electronic correlations in the layered organic metal κ-$(BETS)_2Mn[N(CN)_2]_3$. *Low Temp. Phys.* **43**, 239–243 (2017).
49. Vyaselev, O. M. et al. Properties of Mn^{2+} and π-electron spin systems probed by ^1H and ^{13}C NMR in the organic conductor κ-$(BETS)_2Mn[N(CN)_2]_3$. *Crystals* **2**, 224–235 (2012).
50. Kanoda, K. Electron correlation, metal-insulator transition and superconductivity in quasi-2D organic systems $(ET)_2X$. *Phys. C: Superconduct.* **282–287**, 299 (1997).
51. Toyota, N., Lang, M. & Müller, J. *Low-Dimensional Molecular Metals*. Solid State Science (Springer-Verlag Berlin Heidelberg, 2007).
52. Zverev, V. N. et al. Fermi surface properties of the bifunctional organic metal κ-$(BETS)_2Mn[N(CN)_2]_3$ near the metal-insulator transition. *Phys. Rev. B* **99**, 125136 (2019).
53. Riedl, K., Gati, E. & Valentí, R. Ingredients for generalized models of κ-phase organic charge-transfer salts: a review. *Crystals* 12, (2022).
54. Vyaselev, O. M., Kartsovnik, M. V., Kushch, N. D. & Yagubskii, E. B. Staggered spin order of localized π-electrons in the insulating state of the organic conductor κ-$(BETS)_2Mn[N(CN)_2]_3$. *JETP Lett.* **95**, 565 (2012).
55. Thomas, T. et al. Low-frequency charge carrier dynamics in ferroelectric κ-$(BEDT\text{-}TTF)_2X$: a comparative study of X=$Cu[N(CN)_2]Cl$ and X=$Hg(SCN)_2Cl$. *Phys. Status Solidi B* **256**, 1800746 (2019).
56. Müller, J. & Thomas, T. Low-frequency dynamics of strongly correlated electrons in $(BEDT\text{-}TTF)_2X$ studied by fluctuation spectroscopy. *Crystals* **8**, 166 (2018).
57. Müller, J., Iguchi, S., Taniguchi, H. & Sasaki, T. Formation of nanoscale polarized clusters as precursors of electronic ferroelectricity probed by conductance noise spectroscopy. *Phys. Rev. B* **102**, 100103 (2020).
58. Raquet, B., Anane, A., Wirth, S., Xiong, P. & von Molnár, S. Noise probe of the dynamic phase separation in $La_{2/3}Ca_{1/3}MnO_3$. *Phys. Rev. Lett.* **84**, 4485–4488 (2000).
59. Martin Dressel, private communication (2024).
60. Lunkenheimer, P. et al. Colossal dielectric constants in transition-metal oxides. *Eur. Phys. J. Special Top.* **180**, 61–89 (2009).
61. Bobnar, V., Lunkenheimer, P., Paraskevopoulos, M. & Loidl, A. Separation of grain boundary effects and intrinsic properties in perovskite-like $Gd_{0.6}Y_{0.4}BaCo_2O_{5.5}$ using high-frequency dielectric spectroscopy. *Phys. Rev. B* **65**, 184403 (2002).
62. Cross, L. E. Relaxor ferroelectrics. *Ferroelectrics* **76**, 241–267 (1987).
63. Samara, G. A. The relaxational properties of compositionally disordered ABO_3 perovskites. *J. Phys.: Condens. Matter* **15**, R367–R411 (2003).
64. Viehland, D., Jang, S. J., Cross, L. E. & Wuttig, M. Freezing of the polarization fluctuations in lead magnesium niobate relaxors. *J. Appl. Phys.* **68**, 2916 (1990).
65. H. Fischer, J. K. et al. Relaxor ferroelectricity in the polar M_2P-TCNQ charge-transfer crystal at the neutral-ionic interface. *Physical Review B* **103**, 115104 (2021).
66. Canossa, S. et al. Tetramethylbenzidine-tetrafluoroTCNQ(TMB-$TCNQF_4$): a narrow-gap semiconducting salt with room-temperature relaxor ferroelectric behavior. *J. Phys. Chem. C* **125**, 25816–25824 (2021).
67. Thurn, C. et al. Spin liquid and ferroelectricity close to a quantum critical point in $PbCuTe_2O_6$. *npj Quantum Materials* **6**, 95 (2021).
68. Kennett, M. P., Chamon, C. & Cugliandolo, L. F. Heterogeneous slow dynamics in a two dimensional doped classical antiferromagnet. *Phys. Rev. B* **72**, 024417 (2005).
69. Vugmeister, B. E. Polarization dynamics and formation of polar nanoregions in relaxor ferroelectrics. *Phys. Rev. B* **73**, 174117 (2006).
70. Glazounov, A. E. & Tagantsev, A. K. A breathing model for the polarization response of relaxor ferroelectrics. *Ferroelectrics* **221**, 57–66 (1999).
71. Bogdanovich, S. & Popović, D. Onset of glassy dynamics in a two-dimensional electron system in silicon. *Phys. Rev. Lett.* **88**, 236401 (2002).
72. Jaroszyński, J., Popović, D. & M. Klapwijk, T. Universal behavior of the resistance noise across the metal-insulator transition in silicon inversion layers. *Phys. Rev. Lett.* **89**, 276401 (2002).
73. Kar, S., Raychaudhuri, A. K., Ghosh, A., Löhneysen, H. V. & Weiss, G. Observation of non-gaussian conductance fluctuations at low temperatures in Si:P(B) at the metal-insulator transition. *Phys. Rev. Lett.* **91**, 216603 (2003).
74. Jaroszyński, J., Popović, D. & Klapwijk, T. M. Magnetic-field dependence of the anomalous noise behavior in a two-dimensional electron system in silicon. *Phys. Rev. Lett.* **92**, 226403 (2004).
75. Hartmann, B., Zielke, D., Polzin, J., Sasaki, T. & Müller, J. Critical slowing down of the charge carrier dynamics at the Mott metal-insulator transition. *Phys. Rev. Lett.* **114**, 216403 (2015).
76. Ward, T. Z. et al. Time-resolved electronic phase transitions in manganites. *Phys. Rev. Lett.* **102**, 087201 (2009).
77. Weissman, M. B., Israeloff, N. E. & Alers, G. B. Spin-glass fluctuation statistics: mesoscopic experiments in Mn. *J. Magnet. Magn. Mater.* **114**, 87 (1992).
78. Yu, C. C. Why study 1/f noise in Coulomb glasses. *Phys. Stat. Solidi C Curr. Top.* **1**, 25–28 (2004).
79. Yu, C. C. Why study noise due to two level systems: a suggestion for experimentalists. *J. Low Temp. Phys.* **137**, 251–265 (2004).
80. Weissman, M. B. 1/*f* noise and other slow, nonexponential kinetics in condensed matter. *Rev. Mod. Phys.* **60**, 537 (1988).
81. Hassan, N. et al. Evidence for a quantum dipole liquid state in an organic quasi-two-dimensional material. *Science* **360**, 1101–1104 (2018).
82. Urai, M. et al. Anomalously field-susceptible spin clusters emerging in the electric-dipole liquid candidate κ-$(ET)_2Hg(SCN)_2Br$. *Sci. Adv.* **8**, eabn1680 (2022).
83. Chen, Z. & Yu, C. Measurement-noise maximum as a signature of a phase transition. *Phys. Rev. Lett.* **98**, 057204 (2007).
84. Daptary, G. N. et al. Conductivity noise across temperature-driven transitions of rare-earth nickelate heterostructures. *Phys. Rev. B* **100**, 125105 (2019).
85. Pinterič, M. et al. Anisotropic charge dynamics in the quantum spin-liquid candidate κ-$(BEDT\text{-}TTF)_2Cu_2(CN)_3$. *Phys. Rev. B* **90**, 195139 (2014).
86. Fisher, D. S. & Huse, D. A. Nonequilibrium dynamics of spin glasses. *Phys. Rev. B* **38**, 373–385 (1988).
87. Fisher, D. S. & Huse, D. A. Equilibrium behavior of the spin-glass ordered phase. *Phys. Rev. B* **38**, 386–411 (1988).
88. Weissman, M. B. What is a spin glass? A glimpse via mesoscopic noise. *Rev. Mod. Phys.* **65**, 829 (1993).
89. Russell, E. V. & Israeloff, N. E. Direct observation of molecular cooperativity near the glass transition. *Nature* **408**, 695–698 (2000).
90. *The Scaling of Relaxation Processes*, ch. Glassy Dynamics: From Millihertz to Terahertz (Springer Cham. 2018).
91. Kartsovnik, M. Radio-frequency dielectric measurements at temperatures from 10 to 450 K. *Chem. Rev.* **104**, 5737–5781 (2004).
92. Kogan, Sh. Electronic Noise and Fluctuations in Solids (Cambridge University Press: Cambridge, UK, 1996).
93. Müller, J. Fluctuation spectroscopy: a new approach for studying low-dimensional molecular metals. *ChemPhysChem* **12**, 1222 (2011).
94. Pott, R. & Schefzyk, R. Apparatus for measuring the thermal expansion of solids between 1.5 and 380K. *J. Phys. E: Sci. Instrum.* **16**, 444–449 (1983).
95. Böhmer, R., Maglione, M., Lunkenheimer, P. & Loidl, A. Radio-frequency dielectric measurements at temperatures from 10 to 450 K. *J. Appl. Phys.* **65**, 901–904 (1989).

Acknowledgements
We acknowledge support from the Deutsche Forschungsgemeinschaft (DFG, German Research Foundation) through the Transregional Collaborative Research Center TRR 288 - 422213477 (projects A06 and B02). Work in Augsburg was supported by the DFG through TRR 80. M.K. acknowledges support by the DFG through grant no. KA 1652/5-1.

Author contributions
J.M. and M.K. conceived the project. N.K., M.K. and S.M.W. synthesized and provided the single crystals. T.T., Y.A. and J.M. performed and analyzed noise spectroscopy, S.H. and M.L. performed and analyzed thermal expansion measurements, S.S. and P.L. performed and analyzed the dielectric spectroscopy measurements. J.M. coordinated the study. T.T., Y.A., P.L., M.L. and J.M. wrote the manuscript with input from all authors.

Funding
Open Access funding enabled and organized by Projekt DEAL.

Competing interests
The authors declare no competing interests.

Additional information
Supplementary information The online version contains supplementary material available at https://doi.org/10.1038/s44306-024-00022-7.

Correspondence and requests for materials should be addressed to Jens Müller.